

Turbulence Characteristics in a Tidal Channel

YOUYU LU,* ROLF G. LUECK, AND DAIYAN HUANG

School of Earth and Ocean Sciences, University of Victoria, Victoria, British Columbia, Canada

(Manuscript received 28 January 1999, in final form 3 May 1999)

ABSTRACT

A broadband ADCP and a moored microstructure instrument (TAMI) were deployed in a tidal channel of 30-m depth and with peak speeds of 1 m s^{-1} . The measurements enable us to derive profiles of stress, turbulent kinetic energy (TKE), the rate of production and dissipation of TKE, eddy viscosity, diffusivity, as well as mixing length, and to test the parameterization of dissipation rate in the model of Mellor and Yamada. At middepth in the channel where the influence of stratification was present, the Ellison length agrees with the Ozmidov length. The measured mixing length is smaller than the simple z -dependence formulation proposed for unstratified turbulence. The diffusivity of density and heat, and the viscosity for momentum, are correlated and comparable in magnitudes. The 20-min averaged production rate deduced from the ADCP agrees with the dissipation rate estimated from microstructure measurements. The dissipation rate calculated with the Mellor–Yamada model agrees with the measured values with TAMI, but the empirical constant B_1 derived from the data is larger than that conventionally used in the model. In the near-bottom layer, there is a tight correlation between the production rate and the closure-based dissipation rate. The Reynolds stress at 3.6 m above the bottom is consistently 2.5 times smaller than the shear velocity squared (u_*^2), which is inferred from fitting the velocity profiles to a logarithmic form. A logarithmic velocity profile almost always exists and reaches heights of 5.6 to 20 m, but the Reynolds stress is seldom constant in any part of the logarithmic layer.

1. Introduction

Our ability to predict the behavior of coastal environments depends largely on our understanding of the flow and mixing processes. Deriving the flow and turbulence characteristics from measurements is important for understanding coastal dynamics and the development of numerical models. Turbulence measurements are few compared to the vast pool of mean flow data. The important turbulent quantities of practical interest are the frictional force on the flow, turbulence intensity, and various coefficients describing the mixing of momentum and scalars. Turbulent quantities undergo complicated variations in space and time. A turbulent boundary layer is formed above the seabed by bottom friction. Within the boundary layer the flow is attenuated, the shear and frictional force are enhanced, and the turbulent kinetic energy (TKE) production is intensified. The height of the boundary layer is proportional to the scale of turbulent velocity (e.g., Bowden 1978), and can ex-

tend over the whole water depth in shallow seas (Soulsby 1983). It is generally believed that the structure of the oceanic boundary layer bears many similarities to that in atmospheric and laboratory flows. More evidence, particularly from the oceanic boundary layer, is required to convincingly establish this analogy.

In general, numerical models need to parameterize turbulence, partly due to the constraint of computers and partly due to the classical problem that the equations for turbulent moments are not closed. Turbulent closure schemes are commonly based upon scaling arguments and contain constants that must be determined from measurements. Mellor and Yamada (1974, 1982) proposed an hierarchy of turbulent closure models for geophysical boundary layer flows, and their level-2.5 version has been implemented in practical modeling of coastal water circulation (e.g., Blumberg and Mellor 1987; Lynch et al. 1996). The feasibility of this closure scheme and the values of the empirical constants need to be tested by oceanic measurements. Whereas turbulent parameterization can be indirectly tested by the ability of a model to reproduce the mean flow field, a more critical test is the ability to describe the depth dependence and time evolution of turbulence (Simpson et al. 1996).

In this paper, we present an analysis of the turbulent quantities from measurements in a tidal channel with flow magnitudes that are typical for coastal waters. The

* Current affiliation: Department of Oceanography, Dalhousie University, Halifax, Nova Scotia, Canada.

Corresponding author address: Rolf Lueck, School of Earth and Ocean Sciences, University of Victoria, P.O. Box 1700, 3800 Finnerty Road, Victoria, BC V8W 2Y2, Canada.
E-mail: rlueck@uvic.ca

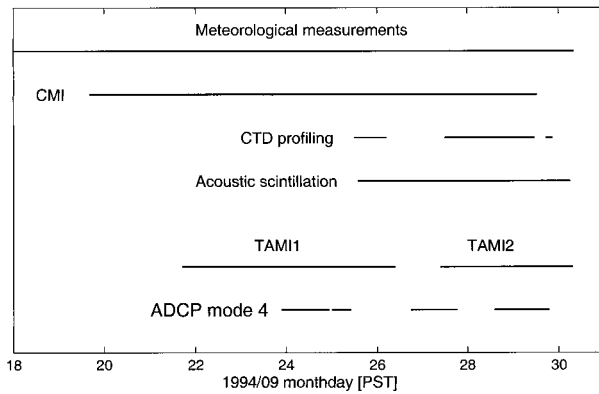


FIG. 1. Duration of measurements made in Cordova Channel with various instruments.

data describe the vertical variation and temporal evolution of turbulence in a tidal boundary layer and are used to test a major parameterization in the Mellor–Yamada model, the closure for dissipation rate. In section 2, we describe the experiment and background measurements made in the study area. In section 3, we introduce the turbulence measurements made with a broadband acoustic Doppler current profiler (ADCP) and a moored microstructure instrument. Section 4 provides a brief account of turbulence parameterization. In section 5, we describe the variations of turbulence throughout the water column based on measurements with the ADCP. Sections 6 and 7 present a quantitative analysis of turbulent characteristics at middepth and in the near-bottom layer, respectively. Section 8 is a summary of the results of this study.

2. Study area and experiment

Cordova Channel is a side channel among a series of narrow passages that link Juan de Fuca Strait to the Strait of Georgia (between Vancouver Island and the mainland of North America). There is a substantial estuarine circulation in this area due to the runoff from several rivers, of which the Fraser River is the largest. The tidal flow is strong in this area and the mixing that it generates in channels and narrow passages influences the estuarine circulation (e.g., Thompson 1981; Foreman et al. 1995).

A multi-investigator experiment in Cordova Channel was conducted in the early fall of 1994 from 19 to 30 September. Most of the data analyzed in this paper are from instruments deployed in the narrowest part of the channel, where it is about 1 km wide and 30 m deep (Lu and Lueck 1999a, Fig. 1). The eastern boundary (James Island) is smoothly curved. The western side is smooth and straight south of the measurement site but the channel broadens northward due to Cordova Spit and Saanichton Bay. The influence of coastline curvature has been noted previously and will be discussed further in this paper.

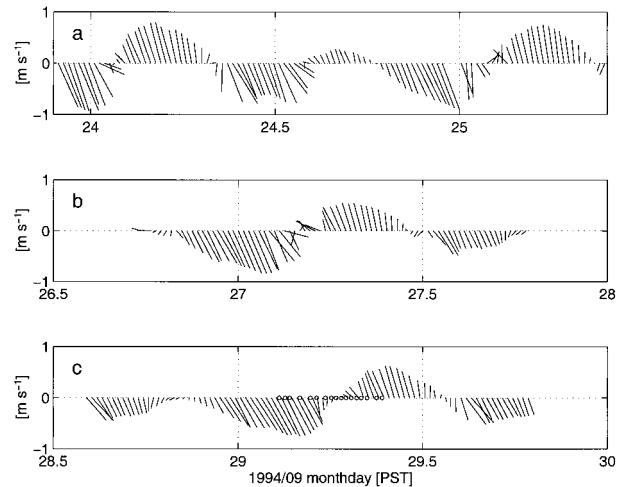


FIG. 2. Stick diagrams of the 20-min mean velocity measured by the ADCP and averaged over the profiling range. Open circles in panel (c) mark the time of the 17 density profiles shown in Fig. 5.

The two instruments deployed by our group are a 600-kHz broadband ADCP and the tethered autonomous microstructure instrument (TAMI) (Lueck et al. 1997; Lueck and Huang 1999). Figure 1 summarizes the duration of all measurements.

Throughout the experiment, the wind speed was typically less than 3 m s^{-1} and reached 5 m s^{-1} only occasionally. The wind stress on the sea surface was negligible compared to the frictional stress at the bottom. The water surface was calm and the wave heights did not exceed 0.2 m during the experiment, according to our visual observation.

A multibeam survey indicates a smooth bottom along the axis of the channel with random undulations of less than 0.1 m peak to peak. The ADCP was at a “high” point in the channel and the bottom slope was 0.015 and 0.01 to the south and north, respectively, for a distance of 200 m. There are small ripples of amplitude 0.1 m at 200 m on either side of the ADCP. The cross-channel slope on the west side of the channel (between isobaths of 15 and 35 m) has many crevices that are irregularly spaced, about 1 m deep and 20 m wide. Divers reported that the bed was composed mainly of fine gravel with diameters ranging from 2 to $8 (\times 10^{-3} \text{ m})$, and the bed contained neither mud nor silt.

The flow in the channel was mainly tidal, directed northward during the flood and southward during the ebb (Lu and Lueck 1999a). During the experiment, the tide changed from spring to neap, and the diurnal constituents became increasingly dominant. Figure 2 provides the time variations of the depth-mean flow for the 3.8 days of ADCP measurements. During these three intervals, the ADCP collected velocity profiles every 3 seconds. An asymmetry between ebb and flood was observed (Lu and Lueck 1999a). The ebb tide was complicated due to the influence of Cordova Spit and the shallows of Saanichton Bay. During the ebb, there were

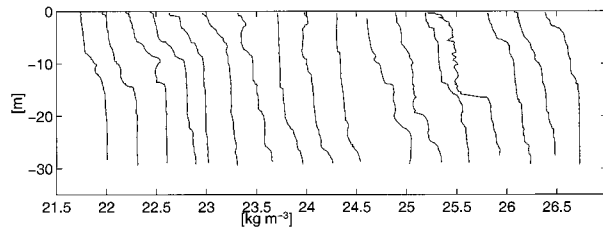


FIG. 3. Consecutive profiles of (σ_t) , in units of kg m^{-3} collected at the south end of Cordova Channel during the interval indicated by open circles in Fig. 2. Successive profiles are shifted by 0.3 kg m^{-3} to the right.

frequent reversals of streamwise shear, fluctuations of flow direction, strong secondary circulation, and transverse shear. During the flood, the flow above the ADCP was nearly aligned with the channel axis and it was only weakly affected by the curvature of the western shore and the shallows.

CTD profiles were taken nominally every 20 min during the period shown in Fig. 1, from the CSS *Vector* anchored near the south entrance of the channel (about 1.5 km to the south of the ADCP). Figure 3 shows 17 consecutive density (σ_t) profiles over one-half semidiurnal tidal period from day 29.1 to 29.4. The stratification varied with time and it correlated with the variation of flow strength (cf. Fig. 2c). During strong flows, the density gradient was larger above than below mid-depth, and unstable overturns were observed during the ebb. During slack current the whole water column was stratified. The effects of stratification on turbulence will be examined in section 6, using the density gradient measured by CTDs mounted on TAMI.

3. Turbulence measurements

a. ADCP

The ADCP was mounted in a quadripod on the seafloor and the steady readings from its tilt sensors indicate that the instrument remained motionless during the experiment. The ADCP measured velocities along its four inclined beams, and the data were transferred via a cable to a computer on shore. About 3.8 days of rapidly sampled velocity data were collected with the standard working mode (mode 4). The data span a range of 25 m [3.6 to 27.6 mab (meters above bottom)] with a vertical resolution of 1 m.

The along-beam velocities, denoted by (b_1, b_2, b_3, b_4) , are low-pass filtered at a cutoff period of 20 min to separate the mean (tidal) and turbulence components. The difference and sum of the turbulent components, namely (b'_1, b'_2, b'_3, b'_4) , provide estimates of two-components of the Reynolds stress and a quantity Q . The formulas used for the calculation are

$$\overline{(u'w', v'w')} = \frac{1}{2 \sin \theta} (\overline{b_1'^2} - \overline{b_2'^2}, \overline{b_3'^2} - \overline{b_4'^2}), \quad (1)$$

$$Q = \frac{1}{4 \sin^2 \theta} (\overline{b_1'^2} + \overline{b_2'^2} + \overline{b_3'^2} + \overline{b_4'^2} - 4D), \quad (2)$$

where $\theta = 30^\circ$ is the beam inclination angle and D is the bias in the variances of the along-beam velocities due to Doppler noise. The combination of the Reynolds stress and mean shear provides estimates of the TKE production rate

$$P = -\left(\overline{u'w'} \frac{\partial u}{\partial z} + \overline{v'w'} \frac{\partial v}{\partial z} \right). \quad (3)$$

The quantity Q is related to the TKE density $q^2/2 = (\overline{u'^2} + \overline{v'^2} + \overline{w'^2})/2$ by

$$Q = \gamma q^2/2, \quad (4)$$

where the factor $\gamma = (1 + 2\alpha \tan^{-2} \theta)/(1 + \alpha)$ is determined by the anisotropy, $\alpha = \overline{w'^2}/(\overline{u'^2} + \overline{v'^2})$. The value of γ ranges from 1 to 2.7, corresponding to $\alpha = 0$ (extremely anisotropic turbulence) to $\alpha = 0.5$ (isotropic turbulence). In this analysis we use $\gamma = 1.8$, hence $\alpha = 0.2$, which is the value estimated by Stacey (1996) from measurements in an unstratified tidal channel.

This technique of estimating turbulent quantities with the variances of ADCP velocities has been reported by Lohrmann et al. (1990), Stacey (1996), Lu (1997), and Lu and Lueck (1999b). Stacey et al. (1999) pointed out that the profiling resolution must be smaller than the sizes of the energy-containing eddies. Estimates of the turbulence length scales are required to determine if this is true.

b. The moored instrument

The moored microstructure instrument TAMI was deployed twice during the experiment at a nominal depth of 15 m. The turbulent velocity and temperature fluctuations were measured, respectively, by shear probes and fast thermistors mounted on TAMI. The TKE dissipation rate, ϵ , were estimated by fitting the velocity spectra to the theoretical spectra in the inertial subrange (Huang 1996; Lueck and Huang 1999). The temperature spectra $\psi(k)$ provide estimates of the weighted-mean temperature spectral level

$$\zeta = \overline{\psi(k) k^{5/3} \epsilon^{1/3}}, \quad (5)$$

where the overbar denotes an average over the inertial-convection subrange. The dissipation rate of temperature fluctuation variance, 2χ , is related to ζ by

$$\chi = \zeta/\beta, \quad (6)$$

where β is a constant. This constant ranges between 0.35 to 1.15 (e.g., Gargett 1985). Following Edson et al. (1991), we choose $\beta = 0.79$ in this study.

4. Turbulence parameterization

a. Mixing coefficients and length scales

The effects of turbulence in transferring momentum and in mixing scalars are usually parameterized by introducing viscosity and diffusivity coefficients. In this study, the measurements with the ADCP and TAMI enable us to get three estimates of the vertical viscosity and diffusivity coefficients, namely

$$A_v = \frac{P}{S^2}, \quad K_v^\rho = \frac{\Gamma\epsilon}{N^2}, \quad K_v^T = \frac{2\chi}{(\partial T/\partial z)^2}, \quad (7)$$

where A_v is the vertical eddy viscosity and K_v^ρ and K_v^T are, respectively, the vertical diffusivity for density and heat. The profiles of A_v are derived from the production rate and mean shear (S) measured with the ADCP. The time series of K_v^ρ and K_v^T are derived from the quantities measured with TAMI, where N is the buoyancy frequency, Γ is the mixing efficiency, and $\partial T/\partial z$ is the mean vertical gradient of temperature. In oceanic environments, Γ varies between 0.04 and 0.4 (Peters et al. 1995) and is typically ≤ 0.2 (Osborn 1980). The estimates of K_v^T are based on assuming a local balance between the rates of dissipation of temperature fluctuation variance, 2χ , and its production (Osborn and Cox 1972).

The turbulent length scales derived from the measurements are the mixing length

$$l_m = \left(\frac{P}{S^3}\right)^{1/2} \quad (8)$$

and the Ozmidov scale

$$l_o = \left(\frac{\epsilon}{N^3}\right)^{1/2}. \quad (9)$$

According to Stacey et al. (1999), the mixing length l_m is related to the Ellison length l_E (a scalar analogy to l_m) by $l_E = 3l_m$, and l_E is argued to be the characteristic length of turbulent eddies. In stratified flow, the Ozmidov length, l_o , characterizes the largest possible overturn that turbulence can accomplish (Turner 1973); hence l_o sets an upper limit on l_E . Determining the characteristic length scale of the TKE-containing eddies is also important because the ADCP averages the velocity vertically over 1 m. The variances of the measured velocity fluctuations may be reduced if the size of the TKE-containing eddies is smaller than $O(1 \text{ m})$.

In unstratified wall-bounded turbulent flows the mixing length is proportional to the distance from the wall. In shallow waters, the growth of the eddies is constrained by the presence of both the seabed and surface. A simple z -dependent mixing length, l_z , is sometimes (e.g., Simpson et al. 1996) proposed as

$$l_z = \kappa z \left(1 - \frac{z}{h}\right)^{1/2}, \quad (10)$$

where $\kappa = 0.4$ is von Kármán's constant, h is the total water depth and z is the height above the seabed.

b. The Mellor–Yamada closure model

In an hierarchy of models proposed by Mellor and Yamada (1974, 1982), the turbulent viscosity and diffusivity coefficients are parameterized in terms of the turbulent intensity (q) and a master length scale (l), that is,

$$(A_v, K_v, K_v^q) = (S_m, S_h, S_q)lq, \quad (11)$$

where K_v^q is the diffusivity for TKE, K_v the diffusivity for tracers, and (S_m, S_h, S_q) are three stability functions.

The Mellor–Yamada level-2.5 model carries the governing equation for TKE density, namely

$$\begin{aligned} \frac{\partial}{\partial t} \left(\frac{q^2}{2} \right) + \mathbf{u} \cdot \nabla \left(\frac{q^2}{2} \right) - \frac{\partial}{\partial z} \left[K_v^q \frac{\partial}{\partial z} \left(\frac{q^2}{2} \right) \right] \\ = P - \epsilon - B. \end{aligned} \quad (12)$$

Besides the rates of production (P) and dissipation (ϵ), the additional term on the right-hand side of (12) is the rate of loss of TKE to buoyancy (B). Conventionally, P and B are parameterized by the local vertical shear and density gradient ($P = A_v S^2$, $B = K_v^\rho N^2$). The rate of dissipation is parameterized in the Mellor–Yamada model by

$$\epsilon_{\text{MY}} = \frac{q^3}{B_1 l}, \quad (13)$$

where B_1 is an empirical parameter.

The stability functions were formulated by Galperin et al. (1988) as

$$\begin{aligned} S_m = \frac{(g_2 - g_3 G_h)}{(1 - g_4 G_h)(1 - g_5 G_h)}, \quad S_h = \frac{g_6}{(1 - g_4 G_h)}, \\ S_q = 0.2, \end{aligned} \quad (14)$$

where

$$G_h = -\frac{l^2 N^2}{q^2}, \quad (15)$$

and g_2, \dots, g_6 are empirical constants. The values of these empirical constants were determined by appealing to data from the laboratory and the atmosphere under neutral conditions (Mellor and Yamada 1982). The values cited by Galperin et al. are $g_2 = 0.39327$, $g_3 = 3.0858$, $g_4 = 34.676$, $g_5 = 6.1272$, $g_6 = 0.49393$, and $B_1 = 16.6$.

The Mellor–Yamada closure of the TKE dissipation rate, ϵ_{MY} , and also the stability functions S_m and S_h , can be calculated using q^2 measured with the ADCP, provided that the master length (l) is known. Let us first examine how l is linked to the mixing length in a special case. Defining $\Lambda = q^2/|u'w'|$, we can rewrite (11) as

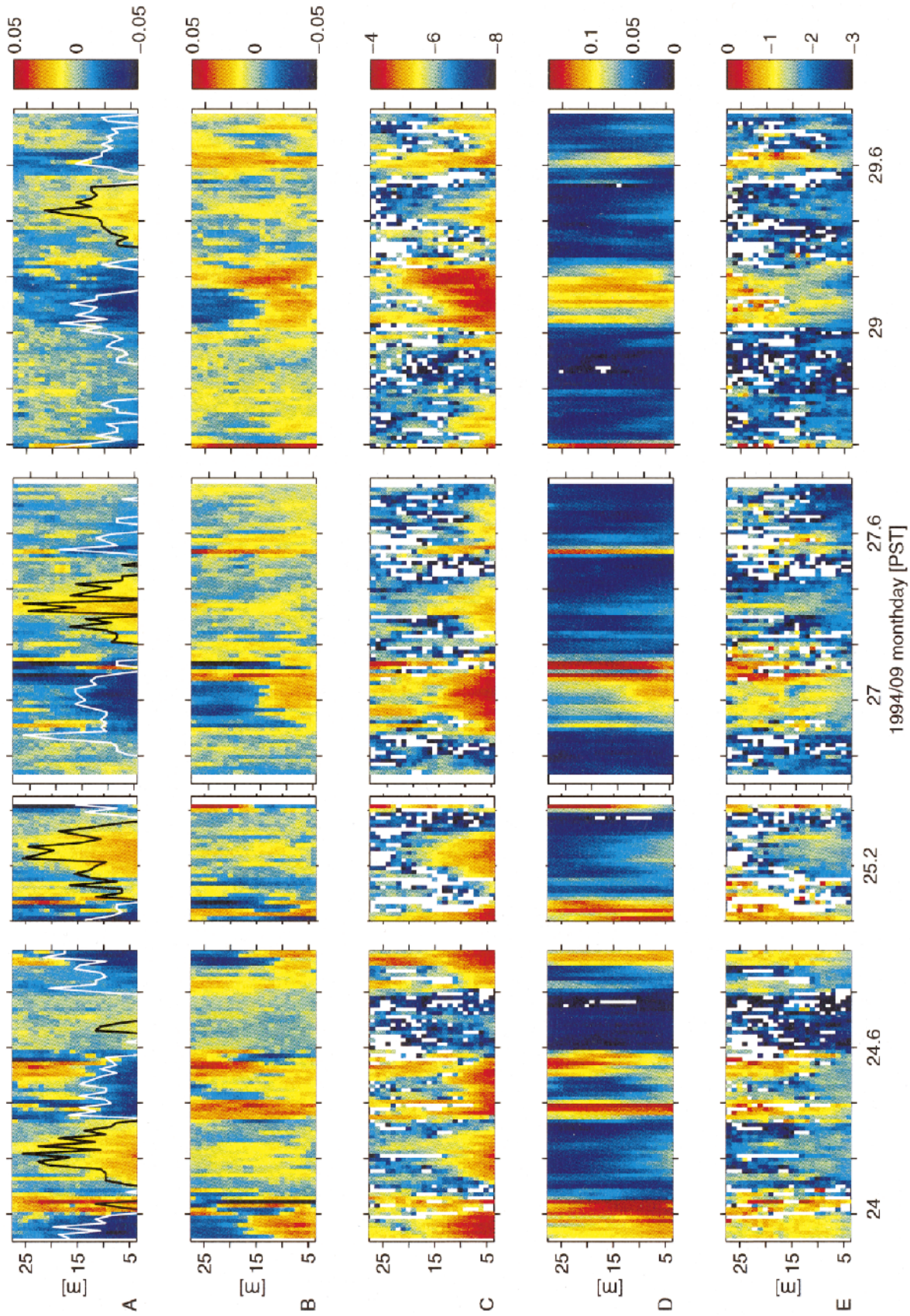


FIG. 4. Depth-time sections of the 20-min mean local friction velocities (a) u_{sp} ($m s^{-1}$), (b) u_{sp} ($m s^{-1}$), (c) $\log_{10}P$ ($m^2 s^{-3}$), (d) q ($m s^{-1}$), and (e) $\log_{10}A_0$ ($m^2 s^{-1}$). The blank areas in (c), (d) and (e) represent negative values. The black (white) curves in panel (a) indicate the height of the log-layer during flood (ebb).

$$l = \frac{1}{S_m} \frac{q}{\Lambda S} \quad (16)$$

and (13) as

$$\epsilon_{MY} = \frac{S_m}{B_1} \Lambda q^2 S. \quad (17)$$

If we choose $l = l_m$, then from (16) S_m is simply

$$S_m = \Lambda^{-1/2}. \quad (18)$$

In the case that the TKE budget (12) is reduced to a balance between the three terms on the right-hand side of (12), that is,

$$P = \epsilon + B = (1 + \Gamma)\epsilon, \quad (19)$$

then combining (17) and (18) gives

$$B_1 = (1 + \Gamma)S_m^{-3}. \quad (20)$$

In the absence of stratification $G_h = \Gamma = 0$; hence $S_m = g_2 = 0.39327$ according to (14) and $B_1 = 16.4$ according to (20). Hence, the values for g_2 and B_1 cited by Galperin et al. (1988) are consistent with assuming $l = l_m$ and that dissipation balances production in unstratified flow. Stacey et al. (1999) argued that the equivalence of l and l_m may also apply in stratified turbulent boundary layers. Following them, we shall set $l = l_m$ to calculate ϵ_{MY} and S_m in this analysis. It is worth noting that according to (20), B_1 is not an universal constant, but rather it varies with changes in S_m and Γ .

5. Depth–time variations of turbulence in the channel

Figure 4 shows the depth-time sections of the 20-min mean estimates of turbulent quantities from measurements taken with the ADCP. Plotted in panels (a) and (b) are the “local friction velocities”

$$u_{*s} = \frac{\overline{(-u'w')}_s}{|\overline{(-u'w')}_s|^{1/2}}, \quad u_{*n} = \frac{\overline{(-v'w')}_n}{|\overline{(-v'w')}_n|^{1/2}}, \quad (21)$$

where $\overline{(-u'w')}_s$ and $\overline{(-v'w')}_n$ are the along- and cross-channel components of the Reynolds stress (the along- and cross-channel directions are defined as parallel and normal to the depth-mean flow, respectively). During the flood, the alongchannel stress is positive (warm shading) and decreases with increasing height. During the ebb, the alongchannel stress is negative (cold shading) and its magnitude also decreases with increasing height, but only in the lower half of the water column. Above middepth, the alongchannel stress frequently reverses sign, corresponding to the sign reversals of the streamwise shear. The cross-channel stress is small during the flood and large during the ebb. This ebb–flood asymmetry of the cross-channel stress reflects the asymmetry of the transverse shear, which is related to variations in the strength of the transverse flow (Lu and Lueck 1999a). The extremely large stress estimates, obtained during the turning of the tide, are unreliable be-

cause these estimates are dominated by single events possibly associated with the large horizontal eddies shed from Cordova Spit (Lu and Lueck 1999b).

The rate of TKE production [panel(c)] intensifies toward the seabed, which is a characteristic of wall-bounded turbulence. However, during the ebb, events of large production occur at heights above the log-layer. These events correspond to the sign reversal of stress (and shear) above middepth and are caused by the entrainment of slower water from the shallows of Saanichton Bay (Lu and Lueck 1999a,b). Negative estimates of P (blank areas) are either due to round-off (and are usually small), or they are caused by unreliable stress estimates obtained during the turning of the tide. The magnitude of P spans about three decades, ranging from $10^{-4} \text{ m}^2 \text{ s}^{-3}$ (W kg^{-1}) near the bottom to $10^{-7} \text{ m}^2 \text{ s}^{-3}$ during weak flows.

Panel (d) shows the turbulent intensity q , calculated by (4) from the estimates of Q . The Doppler noise level (D) is assumed to be uniform and equal to $1.25 \times 10^{-4} \text{ m}^2 \text{ s}^{-2}$, as determined from tests in an inlet with very weak flows (Lu and Lueck 1999b). The Doppler noise should to some extent depend upon the abundance of sound scatters, which may vary with sites and flow conditions. In this analysis, some negative estimates of q [the blank areas in panel (d)], obtained during weak flows, indicate that the Doppler noise may not have always been as large as $1.25 \times 10^{-4} \text{ m}^2 \text{ s}^{-2}$. The TKE decreases with increasing height, similar to the streamwise friction velocity. The largest estimates of q are obtained at the beginning and end of the ebb and the smallest ones are obtained during weak flows.

The eddy viscosity coefficient A_v [panel (e)] is calculated by dividing P with the squares of the shear (7). The variations of A_v range from about $10^{-3} \text{ m}^2 \text{ s}^{-1}$ during weak flows to $0.3 \text{ m}^2 \text{ s}^{-1}$ during strong flows. The eddy viscosity increases with increasing height in the lower half of the water column and reaches a maximum near middepth.

The white curve in panel (a) depicts the height of the log-layer obtained by fitting the streamwise velocity profiles to a logarithmic form with 1% accuracy (Lueck and Lu 1997). During strong flows, the top of the log-layer reaches more than half way to the surface. The height is predicted well by $0.04u^*/\omega$, where u^* is the friction velocity derived from log-layer fitting, and ω is the angular frequency of the dominant tidal constituent, M_2 .

6. Turbulence characteristics at middepth

Both the ADCP and TAMI took measurements at middepth in the channel. The two instruments were apart by about 50 and 100 m during the first and second deployments of TAMI, respectively. The vertical displacement of TAMI was less than $\pm 1 \text{ m}$ (Huang 1996). For the analyses in this section, the measurements from TAMI are averaged into 20-min ensembles, and the

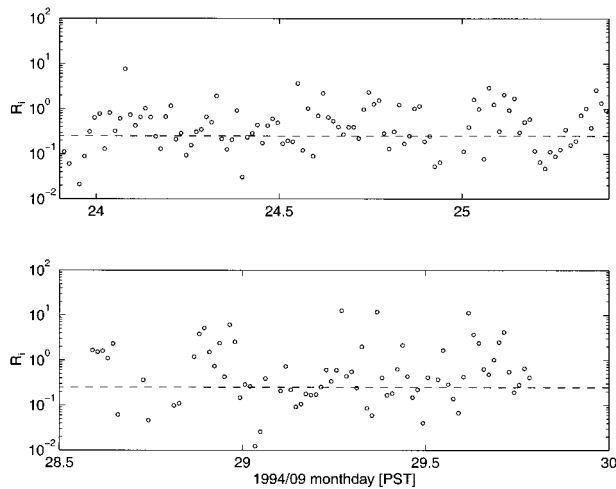


FIG. 5. Estimates of the gradient Richardson number (Ri) at mid-depth using N^2 measured with TAMI and shear measured with the ADCP. Each open circle represents a 20-min average.

quantities estimated with the ADCP are averaged over three levels near middepth over the same 20-min intervals.

According to CTD profiling near the south entrance of the channel (Fig. 3), sharp density gradients occurred mostly near and above middepth during strong flows. At middepth, the moored instrument TAMI carried three CT sensors which the outer pair spaced vertically by 3 m. No shear estimates were available at the site of TAMI; however, we estimate the gradient Richardson number (Ri) by dividing N^2 at TAMI by the shear squared above the ADCP (averaged over 3 m at middepth). A total of 3.2 days of Ri , each value representing a 20-min ensemble mean, are shown in Fig. 5. During the flood, 66% (31%) of the Ri values were greater (less) than $\frac{1}{4}$, and 3% were negative (indication of overturns). During the ebb, 56% (34%) of the Ri values were greater (less) than $\frac{1}{4}$, and 10% were negative. Note that a negative Ri does not mean that the stratification was unstable for the entire 20 minutes represented by a datum. Hence, at middepth, the water column was stable more often than it was unstable during the flood, whereas the chances of stability and instability were roughly equal during the ebb. These statistics of Ri indicates that the influence of stratification cannot be excluded at the middepth.

Figure 6 shows the time series of the Ellison length ($l_E = 3l_m$) and the Ozmidov length (l_o). Both length scales vary significantly with time. The magnitudes of l_E and l_o are comparable. For the total of 3.8 days of data, 34% of the l_E values are negative (due to negative production rate P), the remaining 66% are all greater than 1 m, while 51% are greater than 3 m. Following Stacey et al. (1999), if we take l_E as the characteristic length scale of TKE containing eddies, then all the data points shown in Fig. 8 correspond to eddies with scales larger than 1 m, the vertical resolution of the ADCP.

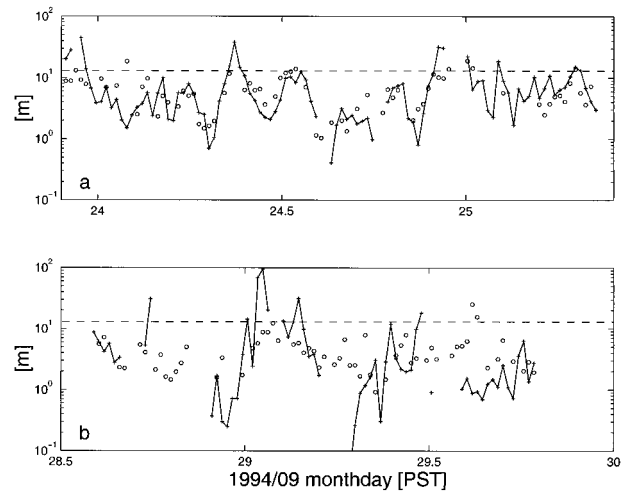


FIG. 6. Time variations of the Ellison length (open circles) and the Ozmidov length (solid lines with crosses) for the two deployments of TAMI. The dashed line depicts $3l_z$, where l_z is the z -dependent mixing length calculated with (10). The quantities are estimated at middepth.

Hence, at middepth, there should not be any reduction of the beam velocity variances due to the vertical averaging of the ADCP. Consequently, we anticipate that the turbulence products are not underestimated at middepth.

At middepth, l_E is generally smaller than $3l_z$. Hence, l_m is smaller than the mixing length $l_z = 4.3$ m (10) based on geometric considerations alone. The reduction of the mixing length from the simple z -dependent formulation can be explained by the influence of stratification, which tends to inhibit the growth of turbulent eddies.

Figure 7 compares the estimates of ϵ from TAMI against the estimates of P from the ADCP. The time

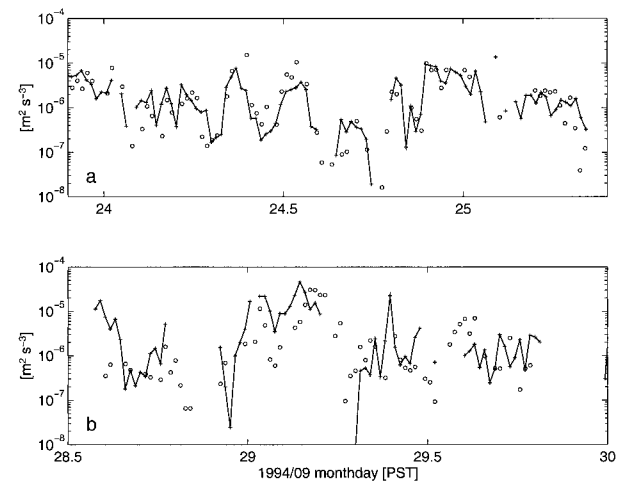


FIG. 7. The rates of TKE dissipation, ϵ , measured with TAMI (solid lines with crosses) vs production, P , (open circles) measured with the ADCP at middepth.

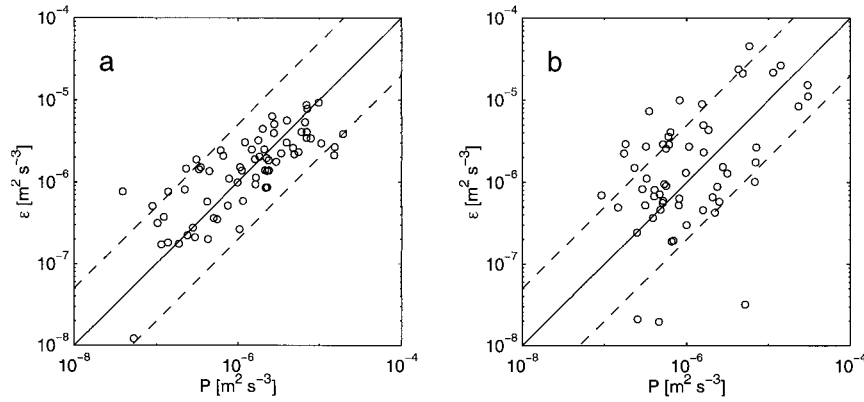


FIG. 8. Scatter diagram of the rates of TKE dissipation vs production at middepth. Panels (a) and (b) present the data from the first and second deployments of TAMI, respectively. Solid line denotes a ratio of 1 and dashed lines represent ratios of 5 and 1/5 between the two quantities.

variations of ϵ correlate well with those of P . The peak values of both rates are about $2 \times 10^{-5} \text{ m}^2 \text{ s}^{-3}$ (W kg^{-1}), and the minimum values are about $2 \times 10^{-8} \text{ m}^2 \text{ s}^{-3}$. Note that during the ebb from day 24.3 to 24.6, both ϵ and P increased by a factor of 30 when the flow direction fluctuated compared to their values between the intervals of fluctuation when the direction was steady (see the stick diagram in Fig. 1). The agreement between the two rates is slightly better during the first deployment of TAMI, probably because the two instruments were closer together. Figure 8 shows a scatter plot of P versus ϵ . During the first deployment of TAMI [panel (a)], almost all of the ϵ values agree with P within a factor of 5, and this is also true for the majority of the ϵ values from the second deployment [panel (b)]. The difference between the estimates of P and ϵ reflects statistical variations more than it does the separation between the two

instruments (e.g., Moum et al. 1995). The agreement is remarkable, considering the two rates are obtained with two completely different instruments using very different sensors.

Figure 9 compares the vertical eddy viscosity coefficient A_v measured with the ADCP against the two diffusivities obtained with TAMI: (a) K_v^p for density and (b) K_v^T for heat. The values of K_v^p are calculated with (7) and using $\Gamma = 0.2$. The agreement between A_v and K_v^p is very good and both ranged between 10^{-3} and $1 \text{ m}^2 \text{ s}^{-1}$. The correlation between A_v and K_v^T is generally good except that K_v^T occasionally has spikes of up to $10 \text{ m}^2 \text{ s}^{-1}$, due to small mean temperature gradients.

Variations of the TKE density, $q^2/2$, and the magnitude of the Reynolds stress $|\overline{u'w'}|$ at middepth are shown in Fig. 10a. There is a clear correlation between the variations of the two quantities. The mean q^2 to $|\overline{u'w'}|$ ratio, Λ , is 12.1 ± 0.9 . Two estimates of the stability

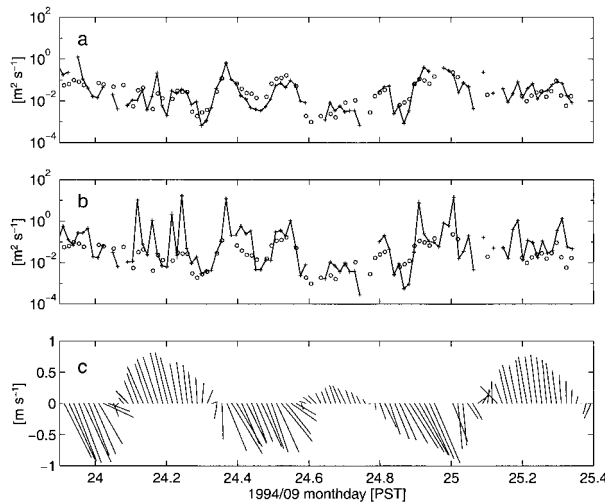


FIG. 9. Time variations of the diffusivity for (a) density (K_v^p) and (b) temperature (K_v^T) (both denoted by solid lines with crosses) compared against the vertical eddy viscosity A_v (open circles, both panels). Panel (c) shows the 20-min flow. All quantities are estimated at middepth.

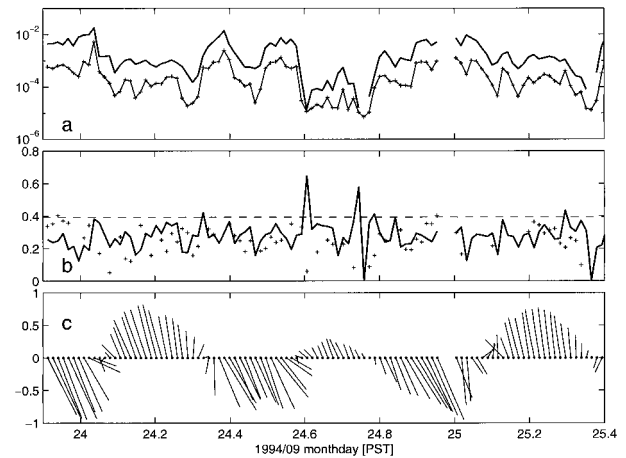


FIG. 10. (a) The TKE density $q^2/2$ (heavy solid lines) vs stress magnitude $\overline{u'w'}$ (thin solid lines with crosses); (b) The stability function S_m calculated using (18) (solid line) and (14) (crosses) vs $S_m = 0.39327$ (dashed line); (c) the stick diagram of the flow. All quantities are estimated at middepth.

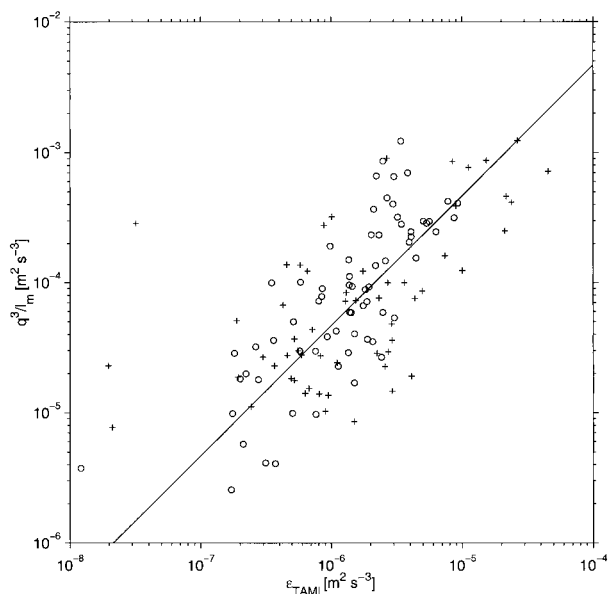


FIG. 11. Scatter diagram of the TKE dissipation rate measured with TAMI against q^3/l_m measured with the ADCP. The factor of proportionality is $B_1 = 46.6$.

function S_m , one calculated with Eq. (14) (assuming $l = l_m$) and the other with (18), are shown in Fig. 10b. Due to stratification, both estimates of S_m are less than 0.393 27, the value in unstratified flow. The mean value of S_m , calculated using (18), is 0.287. The extremely large and small values near day 24.6 and 24.75 are unreliable because they occur just after the start and just before the end of the weak flood when the turbulence was not stationary.

Figure 11 shows a scatter diagram of ϵ measured with TAMI against q^3/l_m measured with the ADCP. A straight line is fitted to the points with the least squares method. The constant of proportionality is B_1 (13), the value required to match the closure-based rate of dissipation ϵ_{MY} to the rate ϵ derived from TAMI. The mean value of B_1 is 46.6 and it has a 95% confidence interval of ± 4.6 , which was obtained using a bootstrap method. The estimate of B_1 may be biased either high or low depending on the degree of isotropy (4). If the anisotropy is even greater than $\alpha = 0.2$, then B_1 is larger than 46.6 and hypothetically as large as 112 for the extreme case of total anisotropy, $\alpha = 0$. Under total anisotropy the flow is no longer turbulent and there is no stress due to the absence of vertical velocity fluctuations. If the isotropy is greater than $\alpha = 0.2$, then B_1 is less than 46.6 and is as small as 23 in the other extreme of complete isotropy, $\alpha = 0.5$. Isotropic turbulence is impossible because there is no stress and, hence, no production of TKE. The smallest possible value of B_1 is still greater than the value of 16.6 cited by Galperin et al. (1988). Correction of the TKE estimates for Doppler noise does not produce a substantial bias because all estimates of TKE are much larger than the noise variance. The re-

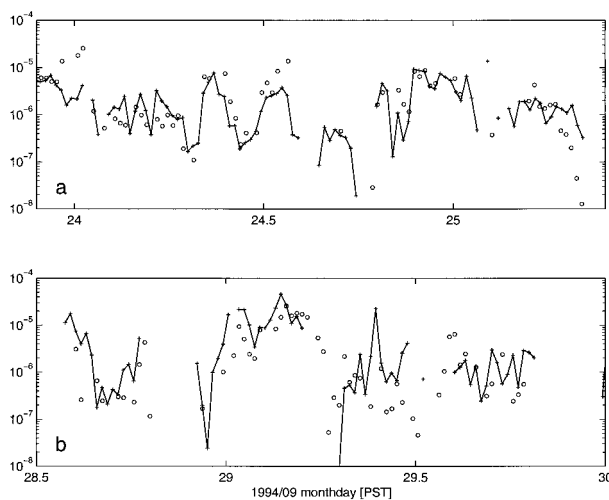


FIG. 12. The rates of TKE dissipation, ϵ , measured with TAMI (solid lines with crosses) vs the dissipation, ϵ_{MY} , calculated using (13) with $l = l_m$ and $B_1 = 46.6$ (crosses).

maining possible explanation for this elevated estimate of B_1 is the influence of stratification, which is unmistakably present at middepth. By assuming $l = l_m$ and a local balance of the TKE budget, (20) predicts an increase of B_1 with a decrease of S_m in a stratified environment, and this is consistent with our estimate of B_1 . Figure 12 compares ϵ from TAMI and ϵ_{MY} calculated with $B_1 = 46.6$ and $l = l_m$. The values track each other well over a range of 2.5 decades and the agreement between ϵ and ϵ_{MY} is slightly but not significantly better than that between ϵ and P (Fig. 7).

At middepth, there are no clear tidal signals in the estimates of the turbulent quantities. Variations of the turbulent parameters appear to be only correlated with changes in TKE density. From Fig. 4c, the region of bottom-enhanced TKE production, which does display a tidal signal, is generally below middepth during the flood. During the ebb, the region of enhanced production protrudes above middepth, but this increase of height is due to the entrainment of water from the shallows of Saanichton Bay into the main stream.

7. Turbulence structure in the near-bottom layer

During strong flows, stratification is weaker in the lower half of the channel than at middepth (Fig. 3). This decrease of N^2 is accompanied by an increase in shear toward the bottom. Hence, the gradient Richardson number should be mostly less than its critical value in the near-bottom layer, and we anticipate that stratification plays a less significant role in suppressing turbulence than at middepth.

Figure 13a shows the time variations of the mixing length l_m at 3.6 mab (the lowest bin of the ADCP). For all 3.8 days of data, 73% of the l_m values are between 0.3 and 1 m, 19% are greater than 1 m, and the remaining

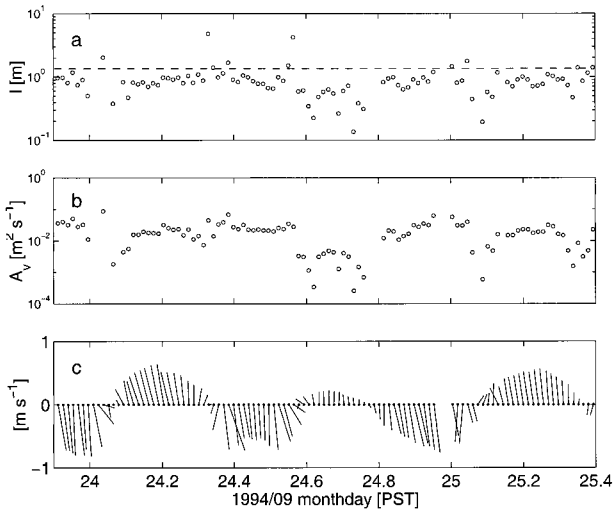


FIG. 13. (a) Mixing length l_m (circles) vs l_e (dashed lines) (in meters) and (b) vertical eddy viscosity A_v ($\text{m}^2 \text{s}^{-1}$). Panel (c) shows a stick diagram of the 20-min flow (m s^{-1}). All quantities are estimates at $z = 3.6 \text{ m}$.

8% are either less than 0.3 m or negative (corresponding to negative production rate). Unlike at middepth, the characteristic length of turbulent eddies ($l_E = 3l_m$) is not significantly greater than the vertical averaging length (1 m) of the ADCP.

Is the Reynolds stress in the near-bottom layer underestimated because of vertical averaging by the ADCP? In the appendix, we analyze additional velocity data that has a vertical resolution of 0.1 m and was collected using the coherent mode of the ADCP. The analysis indicates that spatial averaging reduces the estimated stress by no more than 5%.

Figure 13(b) shows the time variations of the vertical viscosity coefficient A_v . Except during the turning of the tide and during the weak flood between day 24.55 and 24.75, the eddy viscosity is almost independent of flow magnitude at logarithmic scales, ranging between 0.02 and 0.04 $\text{m}^2 \text{s}^{-1}$. During the weak flood, A_v drops to $5 \times 10^{-3} \text{ m}^2 \text{s}^{-1}$ and lower.

Variations of the TKE density and the Reynolds stress are well correlated (Fig. 14a). Both $q^2/2$ and $|u'w'|$ contain clear tidal signals, but they are frequently elevated during the beginning and the end of the ebb when the flow is turning. The mean value of $\Lambda = q^2/|u'w'|$ is 9.84, with a 95% confidence interval of ± 0.61 . The stability function S_m , shown in Fig. 14b, is calculated from the q^2 -to-stress ratio with (18). During strong flows when the magnitudes of the stresses are large, the values of S_m are close to $g_2 = 0.39327$, as predicted by (14) when $N = 0$. By comparing the near-bottom estimates of S_m against those from middepth (Fig. 10b), it is evident that the effects of stratification are weaker near the bottom.

The correlation between q^3/l_m and P at $z = 3.6 \text{ m}$ (Fig. 15) is tight and much closer than that between q^3/l_m and ϵ at middepth (Fig. 11). The constant of pro-

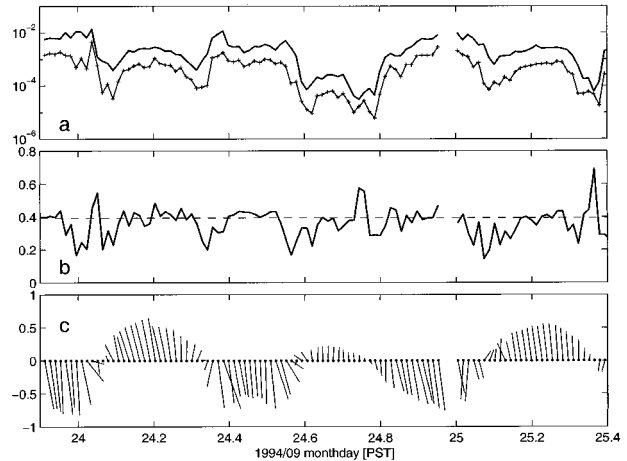


FIG. 14. (a) TKE density, $q^2/2$, (heavy solid lines) vs stress magnitude $|u'w'|$ (thinner lines with crosses) (both in $\text{m}^2 \text{s}^{-2}$). (b) Values of the stability function S_m calculated with (18) (solid line) vs $S_m = 0.39327$ (dashed line); (c) the stick diagram of the flow. All quantities are estimated at $z = 3.6 \text{ m}$.

portionality is $B_1 = 26.3 \pm 1.2$ for speeds exceeding 0.35 m s^{-1} . Matching the rate of production to the rate of dissipation predicted by the Mellor–Yamada closure requires an adjustment of B_1 from 16.6 to 26.3. For $B_1 = 16.6$, the predicted rate of dissipation exceeds the measured rate of production. Given that, on average, (i) the measured rate of production agrees with the measured rate of dissipation at middepth, (ii) the Richardson number is smaller near the bottom than at middepth, (iii) vertical averaging does not significantly reduce the

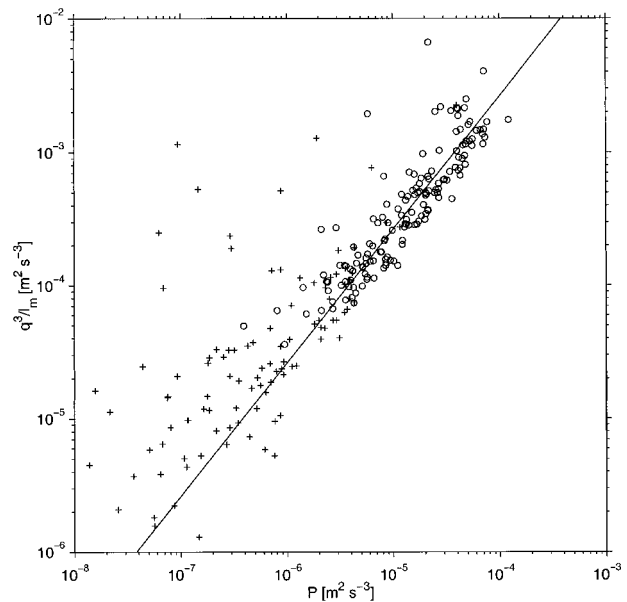


FIG. 15. Scatter diagram of the rate of TKE production against q^3/l_m . Open circles and crosses are for speeds greater than and less than 0.35 m s^{-1} , respectively. The constant of proportionality is $B_1 = 26.3$. All quantities are estimates at $z = 3.6 \text{ m}$.

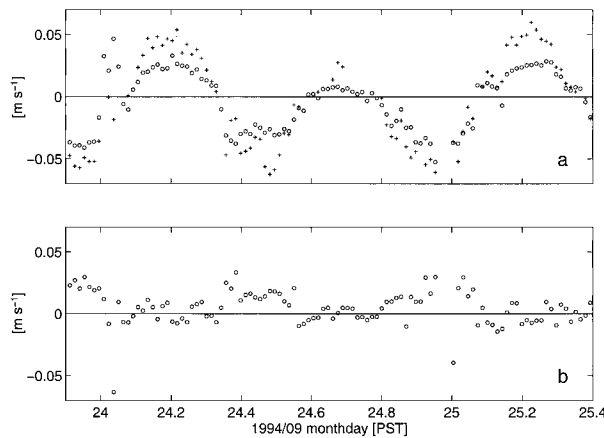


FIG. 16. Time series of local friction velocities (a) u_{*s} and (b) u_{*n} (open circles) at $z = 3.6$ mab, and u_* (crosses) obtained by fitting the streamwise velocity profiles to a log-layer.

estimated stress, and (iv) the rate of production of buoyancy is at most about 20% of the rate of dissipation, then it is unlikely that the rate of dissipation is much less than the rate of production. Uncertainty about the actual degree of isotropy cannot explain the larger than predicted value of B_1 . The estimate of B_1 is biased high if the actual isotropy is larger than $\alpha = 0.2$ because a larger isotropy would increase our estimate of TKE using (4). A larger isotropy is possible, but it would have to be $\alpha = 0.41$ to make our estimate B_1 equal to 16.6 and such a high degree of isotropy is not plausible. The remaining possible explanation for this elevated estimate of B_1 is, like at middepth, the influence of stratification according to (20). Some estimates of S_m are smaller than $g_2 = 0.39$ (Fig. 14b) even when the flow is stronger than 0.35 m s^{-1} . Thus, stratification is not always negligible at 3.6 m.

The along- and cross-channel local friction velocities u_{*s} and u_{*n} at 3.6-m height are shown in Fig. 16. The cross-channel local friction velocity is large during the ebb, with peak values of 0.025 m s^{-1} , but small during the flood. The alongchannel friction velocity reaches 0.04 m s^{-1} during peak flow, corresponding to a streamwise stress magnitude of $1.6 \times 10^{-3} \text{ m}^2 \text{ s}^{-2}$. The magnitude of u_{*s} is, however, consistently smaller than the shear velocity u_* obtained by fitting the streamwise velocity profiles to a log-layer (Lueck and Lu 1997). The mean ratio of u_{*s}^2 to u_*^2 is 0.41; that is, the log-layer-fitted bottom stress is on average larger than the measured alongchannel Reynolds stress by a factor of 2.5. Vertical profiles of the Reynolds stress (not shown) are neither constant nor linear, even within the log-layer.

One possible explanation for the discrepancy $|u'w'|$ and u_*^2 is the influence of horizontal inhomogeneity caused by bedforms. Theoretical analyses (e.g., Belcher et al. 1993) have shown that the turbulent boundary layer over small-scale topographic features can be significantly distorted from the classical boundary layer over smooth walls. However, a factor 2.5 increase of

bottom stress requires sand waves of amplitude 1 m and wavelength 10 m, and there is no evidence for such bedforms in Cordova Channel. The existence of bedforms causes a form drag that influences the flow field farther away from the bottom than does skin friction. In oceanic bottom boundary layers, measurements have revealed the existence of multiple log-layers (Chriss and Caldwell 1982; Sanford and Lien 1999). The bottom stress inferred from fitting the velocity profile in the outer log-layer (extending more than a few meters from bottom, as in this study) likely contains a contribution from form drag, in addition to the local Reynolds stress.

8. Conclusions

A bottom-mounted ADCP and the microstructure instrument TAMI, moored at middepth, measured turbulence, flow, and density stratification in Cordova Channel. The flow in the channel is mainly tidal and with peak speeds of 1 m s^{-1} . The data enable us to derive estimates of Reynolds stress, TKE density, the rates of TKE production and dissipation, eddy viscosity and diffusivity, and turbulence length scales.

Depth-time variations of turbulence in the channel are revealed by measurements with the ADCP. The variation of the Reynolds stress with depth corresponds to the vertical structure of the mean shear. The along-channel component of the stress contains clear tidal variations, but the cross-channel component is only significant during the ebb when the secondary circulation is strong. The production of turbulent kinetic energy is generally enhanced near the bottom, bearing the character of wall-bounded turbulence, but events of large production rate can occur at heights above the log-layer. The TKE density changes more strongly with time than with depth. The eddy viscosity has a maxima at middepth.

The two instruments provided simultaneous measurements at middepth. Statistics of the gradient Richardson number indicate that stratification was important at this depth. Estimates of the Ellison length and Ozmidov length are comparable in magnitude. The mixing length is smaller than that predicted by the simple z -dependent formulation (10), which does not take stratification into account. Two estimates of eddy diffusivity and one estimate of viscosity are obtained. The three estimates are comparable and they correlate over the range of 10^{-3} to $1 \text{ m}^2 \text{ s}^{-1}$. The q^2 to $|u'w'|$ ratio is estimated to be 12.1. Independent estimates of the TKE production and dissipation rates agree within a factor of 5 for 20-min ensembles. Both rates ranged between 2×10^{-8} and $2 \times 10^{-5} \text{ m}^2 \text{ s}^{-3}$.

The stability function S_m in the Mellor–Yamada model, calculated using q^2 and mixing length measured with the ADCP, has a mean value of 0.287, smaller than 0.393 27 for unstratified flow. The measured dissipation rate is proportional to q^3/l_m . By taking the mixing length

l_m as the master length, the dissipation rate calculated with the Mellor–Yamada model is proportional to the rate of dissipation measured with TAMI, and both rates agree if $B_1 = 46.6$. A possible explanation for this large estimate of B_1 (compared to the value of 16.6 in the literature) is the influence of stratification. By assuming $l = l_m$ and a local TKE balance, the relationship between B_1 and S_m based on the Mellor–Yamada closure actually predicts an increase of B_1 with decreasing S_m in a stratified environment.

Close to the bottom, the measured turbulent quantities contain stronger tidal variations than at middepth. The influence of stratification is expected to be small because of the strong shear and weak density gradient. Estimates of the eddy viscosity range between 0.02 and 0.04 m² s⁻¹ and are fairly steady except during the turning of the tide and during very weak flows. The q^2 to $-|u'w'|$ ratio is 9.84 ± 0.61 . The stability function S_m is smaller but closer than at middepth to the value used in the Mellor–Yamada model in unstratified flow. There is a tight correlation between the dissipation rate calculated with the Mellor–Yamada model and the rate of production estimated from the shear and stress. The two rates match for the choice $B_1 = 26.3$.

Although the mean velocity profiles are fitted accurately to a log-layer, the Reynolds stress is not constant within the log-layer. At 3.6-m height, the magnitude of the along-channel stress is smaller than the log-layer fitted bottom stress by a factor of 2.5. Interestingly, Johnson et al. (1994) found a factor of 3 discrepancy between the bottom stress obtained from log-layer fitting and that derived from dissipation estimates using data collected in the Mediterranean outflow. We speculate that form drag causes a discrepancy between the magnitude of the near-bottom Reynolds stress and bottom stress obtained from a fit of velocity to a logarithmic profile.

Acknowledgments. We would like to thank D. Newman and J. Box for their technical support to the field program, and D. Farmer who provided the CTD data. Comments from Steven Monismith and the anonymous reviewers led to significant improvement to the original manuscript. This work was supported by the U.S. Office of Naval Research under Grant N00014-93-1-0362.

APPENDIX

The Influence of Profiling Resolution to Stress Estimates

The profiling range of the ADCP is broken into equally spaced segments called depth cells. The along-beam velocity at each cell is the average of the velocity in a volume that has a cross section equal to that of the transducer and a length equivalent to the cell size. The actual vertical weighting is that of a triangle with 50% overlap between adjacent cells. The concern for tur-

bulence measurement is that the averaging volume should not exceed the size of the energy- and stress-containing eddies. For the results presented above, we used data collected using the standard mode (mode 4) of the ADCP and with 1-m cell size. At 3.6 m above the seabed, the Ellison length is not significantly larger than the cell size and the Reynolds stress may be underestimated due to spatial averaging.

During the experiment, we also collected data using the coherent mode (mode 5) of the ADCP. This mode provides much finer profiling resolution (0.1 m) and lower noise, but at a cost of very limited range ($O(1)$ m). We obtained useful data in eight bins and used these to compare two estimates of the alongstream Reynolds stress. The first estimate, τ_1 , is the average of the stresses at the eight levels, while the second estimate, τ_2 , is the stress obtained from the vertically averaged velocity. The second estimate is a proxy for the results obtained with mode 4. Estimates are obtained for two segments of data that are 34 and 44 minutes long, respectively. For segment 1 $\tau_1 = 8.82$ and $\tau_2 = 8.52$, while for segment 2, $\tau_1 = 9.19$ and $\tau_2 = 8.59$, all in units of 10^{-4} m² s⁻². The ratio of the two estimates is 0.96 and 0.93, and we conclude that the stress derived with 1-m cells is underestimated by only 5% near the bottom.

REFERENCES

- Belcher, S. E., T. M. J. Newley, and J. C. R. Hunt, 1993: The drag on an undulating surface induced by the flow of a turbulent boundary layer. *J. Fluid Mech.*, **249**, 557–596.
- Blumberg, A. F., and G. L. Mellor, 1987: A description of a three-dimensional coastal ocean circulation model. *Three-Dimensional Coastal Ocean Models*, N. S. Heaps, Ed., Coastal and Estuarine Sciences, Vol. 4, Amer. Geophys. Union, 1–16.
- Bowden, K. F., 1978: Physical problems of the benthic boundary layer. *Geophys. Surv.*, **3**, 255–296.
- Chriss, T. M., and D. R. Caldwell, 1982: Evidence for the influence of form drag on bottom boundary layer flow. *J. Geophys. Res.*, **87**, 4148–4154.
- Edson, J. B., C. W. Fairall, P. G. Mestayer, and S. E. Larsen, 1991: A study of the inertial-dissipation method for computing air–sea fluxes. *J. Geophys. Res.*, **96**, 10 689–10 711.
- Foreman, M. G. G., R. A. Walters, R. F. Henry, C. P. Keller, and A. G. Dolling, 1995: A tidal model for eastern Juan de Fuca Strait and the southern Strait of Georgia. *J. Geophys. Res.*, **100**, 721–740.
- Galperin, B., L. H. Kantha, S. Hassid, and A. Rosati, 1988: A quasi-equilibrium turbulent energy model for geophysical flows. *J. Atmos. Sci.*, **45**, 55–62.
- Gargett, A. E., 1985: Evolution of scalar spectra with the decay of turbulence in a stratified fluid. *J. Fluid Mech.*, **159**, 379–407.
- Huang, D., 1996: Turbulent mixing in a tidal channel. M.S. thesis, School of Earth and Ocean Sciences, University of Victoria, 125 pp.
- Johnson, G. C., R. G. Lueck, and T. B. Sanford, 1994: Stress on the Mediterranean outflow plume. Part II: Turbulent dissipation and shear measurements. *J. Phys. Oceanogr.*, **24**, 2084–2092.
- Lohrmann, A., B. Hackett, and L. P. Roed, 1990: High resolution measurements of turbulence, velocity and stress using a pulse-to-pulse coherent sonar. *J. Atmos. Oceanic Technol.*, **7**, 19–37.
- Lu, Y., 1997: Flow and turbulence in a tidal channel. Ph.D. thesis, University of Victoria, 140 pp.
- , and R. G. Lueck, 1999a: Using a broadband ADCP in a tidal

- channel. Part I: Mean flow and shear. *J. Atmos. Oceanic Technol.*, **16**, 1556–1567.
- , and —, 1999b: Using a broadband ADCP in a tidal channel. Part II: Turbulence. *J. Atmos. Oceanic Technol.*, **16**, 1568–1579.
- Lueck, R. G., and Y. Lu, 1997: The logarithmic layer in a tidal channel. *Contin. Shelf Res.*, **17**, 1785–1801.
- , and D. Huang, 1999: Dissipation measurement with a moored instrument in a swift tidal channel. *J. Atmos. Oceanic Technol.*, **16**, 1499–1505.
- , —, D. Newman, and J. Box, 1997: Turbulence measurements with a moored instrument. *J. Atmos. Oceanic Technol.*, **14**, 143–161.
- Lynch D. R., J. T. C. Ip, C. E. Naimie, and F. E. Werner, 1996: Comprehensive coastal circulation model with application to the Gulf of Maine. *Contin. Shelf Res.*, **16**, 875–906.
- Mellor, G. L., and T. Yamada, 1974: A hierarchy of turbulence closure models for planetary boundary layers. *J. Atmos. Sci.*, **31**, 1791–1806.
- , and —, 1982: Development of a turbulence closure model for geophysical fluid problems. *Rev. Geophys. Space Phys.*, **20**, 851–875.
- Moum, J. N., M. C. Gregg, R. C. Lien, and M. E. Carr, 1995: A comparison of turbulent kinetic energy dissipation rate estimates from two ocean microstructure profilers. *J. Atmos. Oceanic Technol.*, **12**, 346–366.
- Osborn, T. R., 1980: Estimates of the local rate of vertical dissipation from dissipation measurements. *J. Phys. Oceanogr.*, **10**, 83–89.
- , and C. S. Cox, 1972: Oceanic fine structure. *Geophys. Fluid Dyn.*, **3**, 321–345.
- Peters, H., M. C. Gregg, and T. B. Sanford, 1995: Detail and scaling of turbulent overturning in the Pacific Equatorial Undercurrent. *J. Geophys. Res.*, **100**, 18 333–18 348.
- Sanford, T. B., and R.-C. Lien, 1999: Turbulent properties in a homogeneous tidal bottom boundary layer. *J. Geophys. Res.*, **104**, 1245–1257.
- Simpson, J. H., W. R. Crawford, T. P. Rippeth, A. R. Campbell, and J. V. S. Cheok, 1996: The vertical structure of turbulent dissipation in shelf seas. *J. Phys. Oceanogr.*, **26**, 1579–1590.
- Soulsby, R. L., 1983: The bottom boundary layer of shelf seas. *Physical Oceanography of Coastal and Shelf Seas*, B. Johns, Ed., Elsevier Oceanogr. Ser., Vol. 35, Elsevier, 189–266.
- Stacey, M. T., 1996: Turbulent mixing and residual circulation in a partially stratified estuary. Ph.D. thesis, Stanford University, 209 pp.
- , S. G. Monismith, and J. R. Burau, 1999: Observations of turbulence in a partially stratified estuary. *J. Phys. Oceanogr.*, **29**, 1950–1970.
- Thompson, R. E., 1981: *Oceanography of the British Columbia Coast*. Canadian Special Publication of Fisheries and Aquatic Science, Series 56, 291 pp.
- Turner, J. S., 1973: *Buoyancy Effects in Fluids*. Cambridge University Press, 367 pp.